The creation of radiation dominated plasmas using laboratory extreme ultra-violet lasers

G J Tallents, S Wilson, A West, V Aslanyan, J Lolley, A K Rossall

York Plasma Institute, Department of Physics, University of York, York YO10 5DD, U.K.

Abstract

Ionization in experiments where solid targets are irradiated by high irradiance extreme ultra-violet (EUV) lasers is examined. Free electron degeneracy effects on ionization in the presence of a high EUV flux of radiation is shown to be important. Overlap of the physics of such plasmas with plasma material under compression in indirect inertial fusion is explored. The design of the focusing optics needed to achieve high irradiance (up to 10^{14} Wcm^{-2}) using an EUV capillary laser is presented.

Keywords: warm dense matter, degenerate plasma, spectroscopy, extreme ultra-violet

1. Introduction

The extreme ultra-violet (EUV) spectral range (10 - 100 nm) has significant potential for a number of applications. EUV radiation is being used to expose photo-resist for the latest generation of computer chip manufacture [1] and purpose-built free electron lasers operating in the EUV have been constructed [2], [3]. A useful laboratory scale laser operating in the EUV at wavelength 46.9 nm has been developed by Rocca et al [4], [5]. This 46.9 nm laser creates output by compressing argon plasma in a capillary confined Z-pinch arrangement. Lasing from Ne-like argon ions on a 3p-3s ($J = 0 - 1$) transition occurs by amplified spontaneous emission with laser output up to 1 mJ energy in pulses of typically 1.5 ns.

The use of EUV lasers for the ablation of small-scale features in solids has been explored [6], [7]. The diameter d_R of a focused laser beam is determined by the wavelength λ of the radiation and the numerical aperture N_A of the focusing optic such that

$$d_R = C_f \frac{\lambda}{N_A} \tag{1}$$

where C_f is a constant varying with the intensity and phase profile of the focused laser beam with a minimum diffraction limited value of $C_f = 2/\pi = 0.64$ for a Gaussian beam. A narrow focus can be formed using EUV lasers due to the combination of the short wavelength of EUV radiation and the ability to create optics with large numerical aperture based on multi-layer mirrors. As well as enabling the ablation of small features for applications, reducing the diameter of beam focus enables higher irradiances to be produced. Harder x-rays typically need to be focused using grazing-incidence optics which limits the maximum numerical aperture possible and the size of focus to a diffraction limited diameter of $\approx 1.5\mu$m [8]. EUV irradiances from capillary lasers are now comparable to some optical laser experiments ($> 10^{10}$ Wcm^{-2}, see [9]), with the potential to achieve irradiances up to 10^{14} Wcm^{-2} with optimised focusing.

The plasma formed by lower irradiance ($< 10^{11}$ Wcm^{-2}) EUV capillary laser irradiation of solid targets has been investigated [7],[9],[10],[11]. The critical electron density for EUV wavelengths in the range 10 - 100 nm ranges from $10^{25} - 10^{23}$ cm^{-3}. Ionised solid materials consequently have electron densities below the critical density, so that the EUV laser light penetrates through ablated, expanding plasma material and can interact directly with material at solid density. Absorption by direct photo-ionization as well as inverse bremsstrahlung occurs. The laser energy is deposited over a longer spatial range and energy deposition is not concentrated near the critical density as occurs with optical laser interactions. Consequently, a greater mass/unit area of material is ablated. With the laser energy spread over a greater mass of material, the temperatures achieved are lower than for optical laser interactions, with significant mass of material at solid density. An EUV laser produces a volume of warm

dense matter which during the laser irradiation has a large flux of incoming radiation (the EUV laser itself).

Indirect drive inertial fusion seeks to produce plasma in the pellet shell and fuel at high density and moderate temperature which is irradiated by a high flux of radiation from within the hohlraum [12]. We are seeking to explore the parallels between the plasmas created in indirect drive inertial fusion and in EUV laser interaction with solids. We have shown that the free electron degeneracy has a dominant role in changing the ionization of plasmas created by EUV radiation if the radiation intensity is sufficiently intense ($> 10^{14}$ Wcm^{-2} [13]). In this paper, we first examine the effects on plasma ionization likely to be observed when photo-ionization dominates the creation of plasma material and then explore some of the experimental issues in creating radiation dominated plasma using capillary laser irradiation of solids.

2. The effects of free electron degeneracy on collisional and radiative processes

We first examine the rates of photo-ionization and three-body recombination in warm dense plasmas. The free electron quantum states can become close to fully occupied which means that the electron energy distribution is given by the Fermi-Dirac distribution rather than a Maxwellian distribution. The full occupancy of free electron quantum states also means that transition rates may be reduced as electrons cannot transition to occupied free electron quantum states. We reduce the transition rates due to electron occupancy by multiplying the necessary cross-sections or rate coefficients by blocking factors of form unity minus the occupancy of the final free electron quantum state.

If the density is high and the temperature of a plasma is low, the chemical potential associated with the near-full occupancy of free electron quantum states is important. The chemical potential of the free electrons is the energy required to add another electron per unit volume to the free electrons. The chemical potential is found, in practise, by integrating the Fermi-Dirac distri-

bution containing the relevant chemical potential, so that the total number of free electrons in unit volume is correct.

As the chemical potential μ is related to the electron density by the requirement that an integration of the electron distribution function over all energies gives the total free electron density n_e, we can write

$$n_e = \int_0^\infty f_{FD}(E)dE = \frac{4}{\sqrt{\pi}} \left(\frac{2\pi m_0 kT}{h^2} \right)^{3/2} I_{1/2}(\mu/kT) \tag{2}$$

where $I_m(\eta_C)$ is the Fermi-Dirac integral of order m. We introduce a reduced chemical potential $\eta_C = \mu/kT$ and write for the Fermi-Dirac integral

$$I_m(\eta_C) = \int_0^\infty \frac{x^m dx}{\exp(x - \eta_C) + 1}. \tag{3}$$

The reduced chemical potential $\eta_C = \mu/kT$ can be determined using equation(2). We plot a scaling of electron density and temperature as a function of the reduced chemical potential η_C (see figure 1). The vertical axis of figure (1) corresponds to constant adiabats.

For indirect drive inertial fusion design studies, the pressure of the imploding fuel relative to the Fermi pressure of degenerate electrons is kept below 1.7 [14] which corresponds to a reduced chemical potential $\eta_C > 1.5$ (see [15]) . For EUV laser-plasmas, we can deduce the chemical potential range from figure (1). Assuming an ionization of Z_{av} per atom and that plasma is formed at material density ρ in units of gcm^{-3}, the electron density in cm^{-3} is given by

$$n_e = \frac{\rho Z_{av}}{1.67A} \times 10^{24} \tag{4}$$

where A is the atomic mass of the target material. Equation (4) and figure (1) show that it is relatively straightforward to create high density plasma material using an EUV laser focused onto a solid target which exhibits a reduced chemical potential in the range of interest for indirect drive inertial fusion. Many elements at room temperature have $\rho/A > 1/6$ gcm^{-3} suggesting from equation (4) that their use as targets for EUV laser ablation can enable electron densities of $n_e \approx 10^{23}$ cm^{-3} with $Z_{av} \approx 1$. For electron temperatures $kT < 20$ eV, the

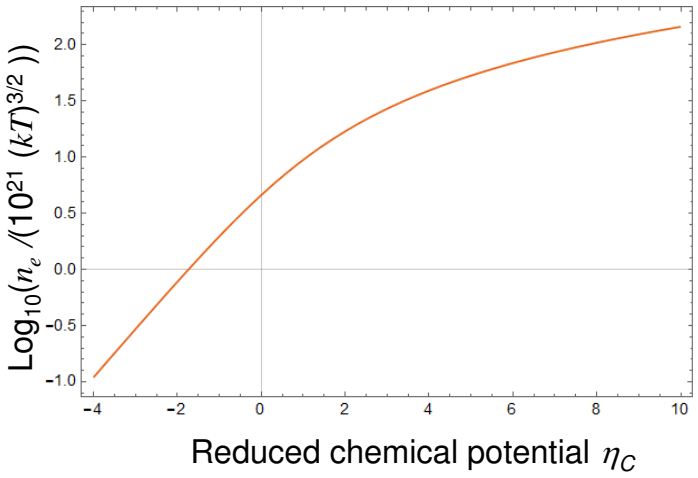

Figure 1: The scaling of electron density n_e in units of cm^{-3} and electron temperature kT in units of eV as a function of the reduced chemical potential $\eta_C = \mu/kT$. At negative chemical potential, the free electron degeneracy is not significant and there is log linear variation.

corresponding reduced chemical potential $N_C > 1.5$. This is the same desired chemical potential range as required for indirect drive inertial fusion.

2.1. Collisional ionization and three-body recombination

A collisional ionization rate coefficient K_{ion} evaluation requires a knowledge of the differential cross-section $\sigma(E, E_1)$ where we assume, say, that the incident electron has an energy E and the ejected electrons have energy E_1 and $E_2 = E - E_1 - E_{ion}$. We can write [15] that

$$K_{ion} N_e = \int_{E_{ion}}^{\infty} \left(\frac{2E}{m}\right)^{1/2} f(E) \left[\frac{\int_0^{E-E_{ion}} \sigma(E, E_1)\ P(E_1)\ P(E_2)\ dE_1}{\int_0^{E-E_{ion}} dE_1}\right] dE \tag{5}$$

where the blocking factors $P(E_1)$ and $P(E_2)$ are appropriate for the two ejected electrons. We assume that the initial bound state has an ionization energy of E_{ion}. The integrations in the square bracket average the differential cross-section and blocking factors over the range of ejected electron energies (from zero energy to the impinging electron energy minus the ionization energy).

We can assume for an approximate treatment that the differential cross-section is constant with ejected electron energy E_1 and simply varies as $\sigma(E, E_1) = \sigma(E_{ion}, 0)E_{ion}/E$. With the assumption that the differential cross-section is independent of the energy distribution between the two electrons, the rate coefficient can be written as

$$K_{ion}N_e \approx \frac{4}{\sqrt{\pi}} \left(\frac{2\pi m}{h^2}\right)^{3/2} \left(\frac{2}{m}\right)^{1/2} E_{ion}\ \sigma(E_{ion}, 0)\ J_{ion}(E_{ion})\ kT \tag{6}$$

with

$$J_{ion}(E_{ion}) = \int_{E_{ion}}^{\infty} \frac{1}{\exp\left(-\frac{\mu - E}{kT}\right) + 1}\ \frac{1}{E - E_{ion}} I_{in}\, dE \tag{7}$$

and

$$I_{in} = \int_0^{\frac{E-E_{ion}}{kT}} \left(1 - \frac{1}{\exp\left(-\frac{\mu - E_1}{kT}\right) + 1}\right) \left(1 - \frac{1}{\exp\left(-\frac{\mu - E_2}{kT}\right) + 1}\right) d(\frac{E_1}{kT}). \tag{8}$$

The inner integral I_{in} is over the blocking factors for the two electrons after the collision. For non-degenerate free electrons, the solution of equation (7) is

$$J_{ion}(E_{ion}) = \exp\left(\frac{\mu - E_{ion}}{kT}\right). \tag{9}$$

For degenerate electrons, we define a ratio R_{ion} for the value of $J_{ion}(E_{ion})$ relative to the low degeneracy value. We have

$$R_{ion} = J_{ion}(E_{ion}) / \left[\exp\left(\frac{\mu - E_{ion}}{kT}\right)\right]. \tag{10}$$

Detailed balance means that the modification to the rate coefficient due to degeneracy for three-body recombination R_{rec} is the same as the modification due to collisional ionization R_{ion}.

We plot the numerically evaluated ratio R_{ion} of the degenerate rate coefficient to the rate coefficient calculated assuming the electrons are non-degenerate in figure (2). The ionization rate coefficient changes by several orders-of-magnitude at high positive chemical potential, but the change is almost independent of the

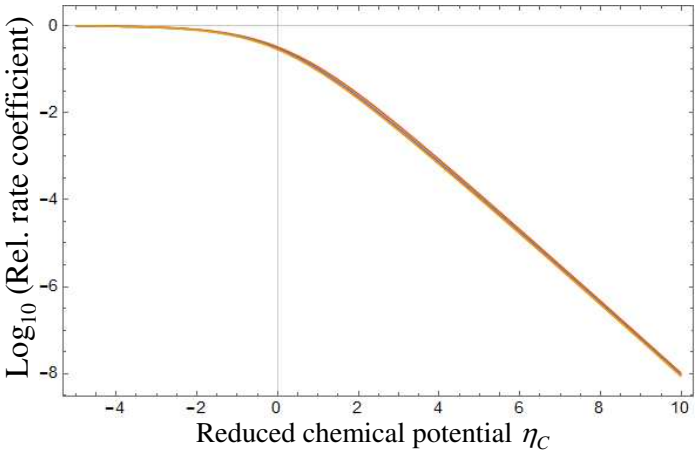

Figure 2: The ratio R_{ion} of the degenerate rate coefficient for ionization (assuming a constant differential cross-section) to the rate coefficient calculated assuming the electrons are non-degenerate. Curves for different ionization energy relative to the electron temperature (β) over the range 0.2 - 1 are plotted but superimpose on top of each other.

electron temperature for a constant value of the reduced chemical potential. Tallents [15] showed that the temperature has a larger effect if the differential cross-section is not assumed to be constant for the different energies of the two electron involved in collisional ionization and three-body recombination and more realistic Mott differential cross-sections are employed. The values of R_{ion} and R_{rec} are also reduced by a moderate amount compared to figure (2) using the Mott differential cross-sections. For example, for $\eta = 5$, the values of R_{ion} and R_{rec} are reduced by approximately a factor 5 in using the Mott cross-section compared to a constant differential cross-section (see figure 3 of Tallents [15]).

2.2. Photo-ionization

Modifications to the rates of photo-ionization can be evaluated by considering the blocking factor for the final energy of the ejected electron. We have for the ratio R^*_{bf} of a photo-ionization cross-section σ^*_{bf} including degeneracy to

the photo-ionization cross-section σ_{bf} without degeneracy:

$$\sigma^*_{bf} = \sigma_{bf} R^*_{bf}$$

where

$$R^*_{bf} = P(E_{ion} - \hbar\omega) = 1 - \frac{1}{\exp\left(-\frac{\mu-(E_{ion}-\hbar\omega)}{kT}\right)+1} \tag{11}$$

where E_{ion} is the ionization energy of the ion. Again detailed balance means that the modification R^*_{fb} due to electron degeneracy of a cross-section for free-bound recombination at the same frequency $\hbar\omega$ is also R^*_{bf}.

2.3. Ionization balance in a radiation dominated degenerate plasma

Consider a radiation dominated plasma where photo-ionization is balanced by three-body recombination. Photo-ionization is the dominant ionization process at irradiances $> 10^{14}$ Wcm^{-2} in the EUV laser irradiance of solid target [13] and can be expected to dominate the ionization of $Z > 1$ ions in the shell and fuel during indirect drive inertial fusion. If the rate coefficient for three-body recombination neglecting degeneracy effects is K_{rec}, then we can write for the populations of two adjacent ionization stages N_Z and N_{Z+1} :

$$n_e N_{Z+1} K_{rec} R_{rec} = N_Z \sigma_{bf} I R^*_{bf} \tag{12}$$

where I is the intensity of the radiation creating the photo-ionization. The population ratio of the two ionization stages is thus given by

$$\frac{N_{Z+1}}{N_Z} = \left(\frac{\sigma_{bf} I}{n_e K_{rec}}\right) \frac{R^*_{bf}}{R_{rec}} \tag{13}$$

so that the ratio R^*_{bf}/R_{rec} represents the effect of degeneracy on the ionization (see figure 3). Provided that photo-ionization dominates collisional ionization (and other processes), the change in the degree of ionization is dominated by the value of the reduced chemical potential as there is little effect with changes of ionization energy (see figure 2). The degree of ionization, however, can change by orders of magnitude at high values of chemical potential.

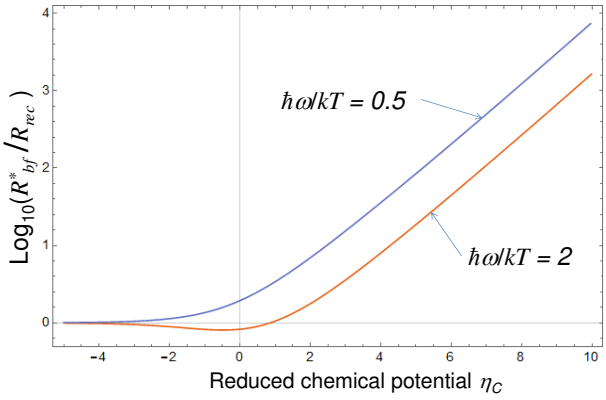

Figure 3: The ratio R^*_{bf}/R_{rec} illustrating the effect of free electron degeneracy on the ionization of a plasma where photo-ionization balances three-body recombination. The relative change due to degeneracy in the ratio of ionization N_{Z+1}/N_Z is shown on a logarithmic scale as a function of reduced chemical potential η_C for an ionization energy equal to the electron temperature at the photon energies of monochromatic incident radiation as labelled.

3. The creation of high EUV laser irradiance

A high numerical aperture focusing geometry is possible in reflection using a Schwarzchild optic as schematically illustrated in figure (4). An optimum Schwarzchild optic consists of two mirrors with radii of curvatures in the ratio ≈ 2.2 and small radii of curvature so that a high numerical aperture can be achieved in the focus. Neglecting diffraction, ray tracing calculations allowing for aberrations show that a focus approximately less than 10^{-5} of the smallest mirror radius of curvature is possible, so that a near-diffraction limited focus is feasible (see figure 5). Figure (5) shows that it is possible to achieve a focused intensity of diameter $\approx 6\lambda \approx 300$ nm with a capillary laser operating at 46.9 nm. The maximum and minimum angles of the radiation to the Schwarzchild axis of symmetry are 150 and 30 milliradians respectively foir figure (5) implying a numerical aperture $N_A = 0.15$. Due to the annular shape of the Schwarzchild focus in near-field, the focusing is not diffraction limited as could

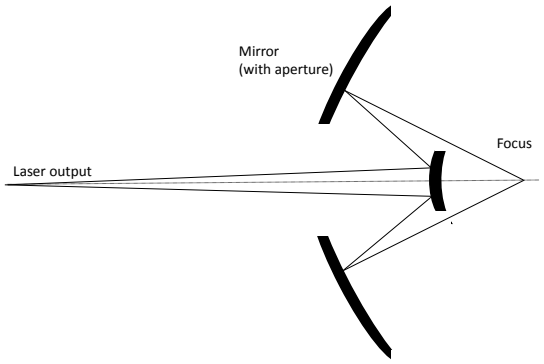

Figure 4: The geometry of a Schwarzchild focusng optic comprising two spherically curved multi-layer mirrors. The geometry is cylindrically symmetric around the dotted line joining the laser output and the focus.

be achieved with a Gaussian beam, so that the constant in equation (1) relating the numerical aperture to the focused beam diameter $C_f \approx 1$.

Multilayer mirrors of scandium and silicon enable reflections of greater than 0.5 for angles of incidence in the range 0 - 20 degrees for 46.9 nm radiation as required for a Schwarzchild optic. Modeling shows that the reflectivity increases with the number of bilayers up to 10 bilayers. Assuming a capillary laser with output of 50 μJ energy, allowing for the reflectivity of two mirrors and assuming a focal spot of 300 nm diameter, can enable focused irradiances of 10^{13} Wcm^{-2}. A more energetic capillary laser with energy output of 1 mJ [5] would enable a focused irradiance of 2×10^{14} Wcm^{-2} so that the ionization balance in an irradiated target would be between photo-ionization and three-body recombination: a radiation dominated ionization balance.

4. Conclusion

Ionization in experiments where solid targets are irradiated by high irradiance extreme ultra-violet (EUV) lasers has been examined. Free electron degeneracy effects on ionization in the presence of a high EUV flux of radiation has been shown to be important. The degree of ionization in plasmas where

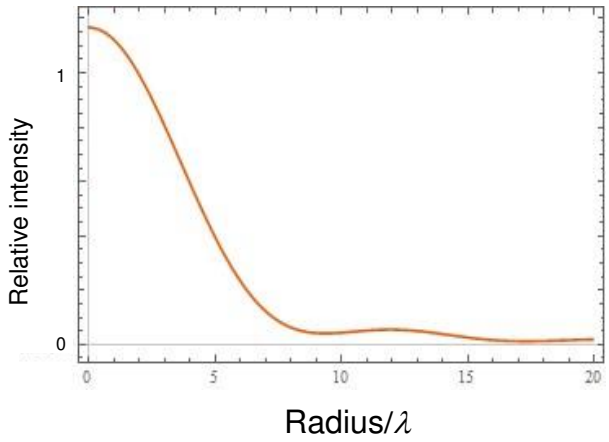

Figure 5: The relative intensity of radiation in the focal plane of a Schwarzchild optic as a function of distance from the optic axis in units of the wavelength of the light. It is assumed that the focused intensity profile is dominated by diffraction effects.

incoming radiation producing photo-ionization is balanced by three-body recombination can be changed by orders-of-magnitude under conditions of high chemical potential as found in warm dense matter. Overlap of the physics of plasmas produced by EUV laser irradiation of solid targets with plasma material under compression in indirect inertial fusion has been explored. The design of the focusing optics needed to achieve high irradiance (up to 10^{14} Wcm^{-2}) using an EUV capillary laser has also been presented.

Acknowledgements

Funding for this work has been provided by a U.K. Engineering and Physical Sciences Research Council grant: Micro-ablation with extreme ulta-violet laser light (administered through Heriot-Watt centre of innovative manufacture in laser-based production processes). We are grateful to Professor Carmen Menoni and Professor Jorge Rocca (Colorado State University) for their collaboration on experiments in this research area.

References

[1] G. Tallents, E. Wagenaars, G. Pert, Optical lithography: lithography at EUV wavelengths, Nature photonics 4 (12) (2010) 809–811. doi:10.1038/nphoton.2010.277.

[2] K. Tiedtke, et al, The soft x-ray free-electron laser FLASH at DESY: beamlines, diagnostics and end-stations, New J. Phys. 11 (2009) 023029. doi:10.1088/1367-2630/11/2/023029.

[3] H. X. Deng, M. M. Zhang, D. Gu, B. Liu, Q. Gu, D. Wang, Simulation studies on laser pulse stability for Dalian coherent light source, Chinese Phys. C 11 (2014) 028101. doi:10.1088/1674-1137/38/2/028101.

[4] J. Rocca, V. Shlyaptsev, F. Tomasel, O. Cortazar, D. Hartshorn, J. Chilla, Demonstration of a discharge pumped table-top soft-x-ray laser, Phy.Rev. Lett. 73 (16) (1994) 2192–2195. doi:10.1103/PhysRevLett.73.2192.

[5] C. Macchietto, B. Benware, J. Rocca, Generation of millijoule-level soft-x-ray laser pulses at a 4-hz repetition rate in a highly saturated tabletop capillary discharge amplifier, Optics Lett. 24 (16) (1999) 1115–1117. doi:10.1016/S0031-8914(53)80099-6.

[6] G. Vaschenko, A. G. Etxarri, C. Menoni, J. J. Rocca, O. Hemberg, S. Bloom, W. Chao, E. Anderson, D. T. Attwood, Y. Lu, B. Parkinson, Nanometer-scale ablation with a table-top soft x-ray laser, Optics Lett. 31 (2006) 3615–3617. doi:10.1364/OL.31.003615.

[7] A. Rossall, V. Aslanyan, G. Tallents, I. Kuznetsov, J. Rocca, C. Menoni, Ablation of submicrometer holes using an extreme-ultraviolet laser, Physical Review Applied 3. doi:10.1103/PhysRevApplied.3.064013.

[8] F. Siewert, J. Buchheim, S. Boutet, G. J. Williams, P. A. Montanez, J. Krzywinski, R. Signorato, Ultra-precise characterization of LCLS hard x-ray focusing mirrors by high resolution slope measuring deflectometry, Optics Express 20 (2012) 4525–4536. doi:10.1364/OE.20.004525.

[9] V. Aslanyan, I. Kuznetsov, H. Bravo, M. R. Woolston, A. K. Rossall, C. S. Menoni, J. J. Rocca, G. J. Tallents, Ablation and transmission of thin solid targets irradiated by intense extreme ultraviolet laser radiation, APL Photonics 1 (2016) 066101. doi:10.1063/1.1578638.

[10] M. Berrill, F. Brizuela, B. Langdon, H. Bravo, C. S. Menoni, J. J. Rocca, Warm photoionized plasmas created by soft-x-ray laser irradiation of solid targets, J. Opt. Soc. Am. B25 (2008) 32. doi:10.1364/JOSAB.25.000B32.

[11] A. Rossall, G. Tallents, Generation of warm dense matter using an argon based capillary discharge laser, High Energy Density Phys. 15 (2015) 67–70. doi:10.1016/j.hedp.2015.04.004.

[12] J. D. Lindl, P. Amendt, R. L. Berger, S. G. Glendinning, S. H. Glenzer, S. Haan, R. Kauffman, O. Landen, L. Suter, The physics basis for ignition using indirect-drive targets on the national ignition facility, Phys. Plasmas 11 (204) 339–491. doi:http://dx.doi.org/10.1063/1.4953669.

[13] V. Aslanyan, G. Tallents, Ionization rate coefficients in warm dense plasmas, Physical Review E 91 (6). doi:10.1103/PhysRevE.91.063106.

[14] S. W. Haan et al, Point design targets, specifications, and requirements for the 2010 ignition campaign on the national ignition facility, Phys. Plasmas 18 (2011) 051001. doi:10.1063/1.3592169.

[15] G. Tallents, Free electron degeneracy effects on collisional excitation, ionization, de-excitation and three-body recombination, High Energy Density Physics 20 (2016) 9–16. doi:10.1016/j.hedp.2016.06.001.